Journal of Biomedical Optics

BiomedicalOptics.SPIEDigitalLibrary.org

Nanoparticle-enabled experimentally trained wavelet-domain denoising method for optical coherence tomography

Irina N. Dolganova
Nikita V. Chernomyrdin
Polina V. Aleksandrova
Sheykh-Islyam T. Beshplav
Alexander A. Potapov
Igor V. Reshetov
Vladimir N. Kurlov
Valery V. Tuchin
Kirill I. Zaytsev

SPIE.

Irina N. Dolganova, Nikita V. Chernomyrdin, Polina V. Aleksandrova, Sheykh-Islyam T. Beshplav, Alexander A. Potapov, Igor V. Reshetov, Vladimir N. Kurlov, Valery V. Tuchin, Kirill I. Zaytsev, "Nanoparticle-enabled experimentally trained wavelet-domain denoising method for optical coherence tomography," *J. Biomed. Opt.* **23**(9), 091406 (2018), doi: 10.1117/1.JBO.23.9.091406.

Nanoparticle-enabled experimentally trained wavelet-domain denoising method for optical coherence tomography

Irina N. Dolganova,[a,b,c,*] Nikita V. Chernomyrdin,[a,b,d] Polina V. Aleksandrova,[a] Sheykh-Islyam T. Beshplav,[e] Alexander A. Potapov,[e] Igor V. Reshetov,[b] Vladimir N. Kurlov,[c] Valery V. Tuchin,[f,*] and Kirill I. Zaytsev[a,b,d,*]
[a]Bauman Moscow State Technical University, Laboratory of Terahert Technology, Moscow, Russia
[b]Sechenov First Moscow State Medical University, Moscow, Russia
[c]Institute of Solid State Physics of RAS, Laboratory of Shaped Crystals, Chernogolovka, Russia
[d]Prokhorov General Physics Institute of RAS, Laboratory of Submillimeter Dielectric Spectroscopy, Moscow, Russia
[e]Burdenko Neurosurgery Institute, Moscow, Russia
[f]ITMO University, Laboratory of Femtomedicine, St. Petersburg, Russia

Abstract. We present the nanoparticle-enabled experimentally trained wavelet-domain denoising method for optical coherence tomography (OCT). It employs an experimental training algorithm based on imaging of a test-object, made of the colloidal suspension of the monodisperse nanoparticles and contains the microscale inclusions. The geometry and the scattering properties of the test-object are known *a priori* allowing us to set the criteria for the training algorithm. Using a wide set of the wavelet kernels and the wavelet-domain filtration approaches, the appropriate filter is constructed based on the test-object imaging. We apply the proposed approach and chose an efficient wavelet denoising procedure by considering the combinations of the decomposition basis from five wavelet families with eight types of the filtration threshold. We demonstrate applicability of the wavelet-filtering for the *in vitro* OCT image of human brain meningioma. The observed results prove high efficiency of the proposed OCT image denoising technique.
[DOI: 10.1117/1.JBO.23.9.091406]

Keywords: optical coherence tomography; wavelet analysis; denoising; filtration; nanoparticles; neuroimaging; meningioma.

Paper 170834SSR received Jan. 5, 2018; accepted for publication Mar. 16, 2018; published online Apr. 11, 2018.

1 Introduction

Since optical coherence tomography (OCT) was introduced by Huang et al.,[1] it has become an effective noninvasive imaging modality mainly in biomedical applications.[2,3] Its effectiveness was shown in ophthalmology[4–8] (especially for diagnostics of retina diseases[5,7–10]), neuroscience,[11–15] vascular and blood imaging,[16,17] dermatology,[18–20] etc. Recent developments in OCT technology show its potential for studying prostate[21] and reproductive organs pathologies,[22] and malignant tissues detection.[13,23–26]

OCT uses the principles of low-coherence interferometry either in time-domain or in frequency-domain.[27–32] Doppler and polarization-sensitive OCT-techniques allow for specific functional and structural tissue imaging.[33] Ongoing development of hardware, such as fiber optics, light sources, mechanical and optical components, used in OCT systems constantly improve image resolution. At the same time, the reliability of OCT measurements can be significantly increased by designing of adequate algorithms for solution of the OCT inverse ill-posed problems.[34–36] However, speckle and scattering noise of the OCT signal prevents the data reconstruction;[37–40] thus, finding an appropriate denoising technique remains one of the challenging problems of OCT technologies.

Nowadays, two general approaches of noise reduction in OCT images are available. The first one is applied during the OCT image acquisition and is based on improvement of the detector integration time or averaging of several scans. The second one involves postprocessing techniques, including filtering, methods of extraction of "pure" signal, and deconvolution procedures.[41] Using more than one OCT scans for noise reduction has a significant drawback for *in vivo* imaging, when object movements become critical. In this case, the averaging should include algorithms of image alignment. Making some assumptions about noise statistics and properties, such methods as independent component analysis,[42] robust principal component analysis,[43] and statistical-based approach[44] give appropriate results, but remain computationally complicated and time-consuming.

Digital filtering as an effective method of noise reduction has been recently implemented in various ways.[9,10,45–51] Since it requires a single OCT image, it can be applied for *in vivo* and *in vitro* biomedical imaging. Median filtration is a common, simple, and quite effective method.[9,47,48] The histogram-based threshold filters show better filtration quality but require knowledge of *a priori* information about the object.[46] For objects with repeatedly appearing features, it is possible to use a nonlocal mean filter with double Gaussian anisotropic kernels,[10] which yields better results in comparison to Wiener, median, and bilateral filters. Effectively used in image formation and processing, wavelet analysis was applied in OCT for noise reduction.[49–52]

*Address all correspondence to: Irina N. Dolganova, E-mail: in.dolganova@gmail.com; Valery V. Tuchin, E-mail: tuchinvv@mail.ru; Kirill I. Zaytsev, E-mail: kirzay@gmail.com

1083-3668/2018/$25.00 © 2018 SPIE

Wavelet kernels and optical wave packets demonstrate similar physical features: zero means value, finite energy corresponding to square norm one, and high locality in both time and frequency domains. The wavelet analysis seems to be optimal for the decomposition of time-domain optical data and, in particular, for the denoising of OCT images.[53] Wavelet analysis employs different types of kernels and filtration methods, thus, choosing the most effective filter parameters for OCT imaging of the particular object of interest remains a challenging problem.

In this paper, we propose the nanoparticle-enabled experimentally trained wavelet-domain denoising technique for OCT. We suggest using a test-object for experimental training, which is made of monodisperse nanoparticle suspension and contains microscale inclusions. To set the criteria for the experimental training of the wavelet-domain denoising procedure, we use information about the geometry and the scattering properties of the test-object, which are known *a priori* and could be tuned with a high precision by changing the nanoparticle size, suspension concentration, geometry and positions of the microscale inclusions. By imaging of the test-object and implementing the wavelet denoising to experimental processing, we choose the appropriate combination of the wavelet decomposition basis and the filtration threshold. We present the results of the experimental demonstration of the proposed technique. In order to show the prospectives of the developed technique for biomedical applications of OCT, we apply it for *in vitro* imaging of human brain meningioma, which seems to be a representative object for the proposed denoising technique. It features a morphologically heterogeneous structure and often contains tumorous cell clusters (whorls) and collagen balls,[13] which could be treated as local microscale inclusions in a semi-infinite scattering space. The observed results demonstrate an ability for denoising of the meningioma OCT images while sustaining all the structural features of biotissues. This justifies high efficiency of the proposed OCT denoising procedure and prospectives of its use in noninvasive and intraoperative medical diagnosis.

2 Nanoparticle-Based Test-Object

We prepare the test-object [see Fig. 1(a)] for the experimental training of the wavelet-domain filter. First, we make a glass cuvette for the test-object, where we place three 80-μm-diameter rigidly fixed cylindrical Cu-wires serving as the microscale inclusions. These wires are placed at the depth of 0.3 mm from the cover window of the cuvette and spaced at the fixed distances of $r_1 = 0.5$ mm and $r_2 = 0.4$ mm measured by visible microscopy. Second, we make aqueous colloidal suspension, i.e., spherical monodisperse nanoparticles of amorphous silica in water. In order to make uniform particle concentration within the suspension volume, we apply ultrasound mixer. We use nanoparticles with diameter of about 400 nm, synthesized by the multistage Stober method.[54,55] Third, we fill the cuvette with the prepared colloidal suspension. During the described preparation of the test-object, we can precisely control its geometrical parameters and scattering properties. These values can be tuned by changing the suspension concentration or/and the positions of the wires. Using the test-object, we can physically simulate OCT imaging of the semi-infinite scattering media with the backscattering inclusions, which is one of the most common cases for many OCT applications.[13]

The quantitative criterion for training of the denoising technique could be based on the prior knowledge of the test-object, for instance, the distances between the reflecting inclusions. In our research, we evaluate an efficiency of the noise reduction by estimating, from the denoised images, the relative distance r_1/r_2 between the wires and comparing it with the actual value $(r_1/r_2)_0 = 1.25$. We perform imaging of the test-object using the OCT system OCT1300Y (Institute of Applied Physics RAS, Nizny Novgorod, Russia), described in detail in Refs. 35, 56, and 57. The experimental setup operates in the near-infrared range and employs laser radiation with the central wavelength of 1.3 μm and the average power of 0.75 mW. It yields A- and B-scans of the sample and produces the 256 × 400 pixel images with the 4-s acquisition time. The declared

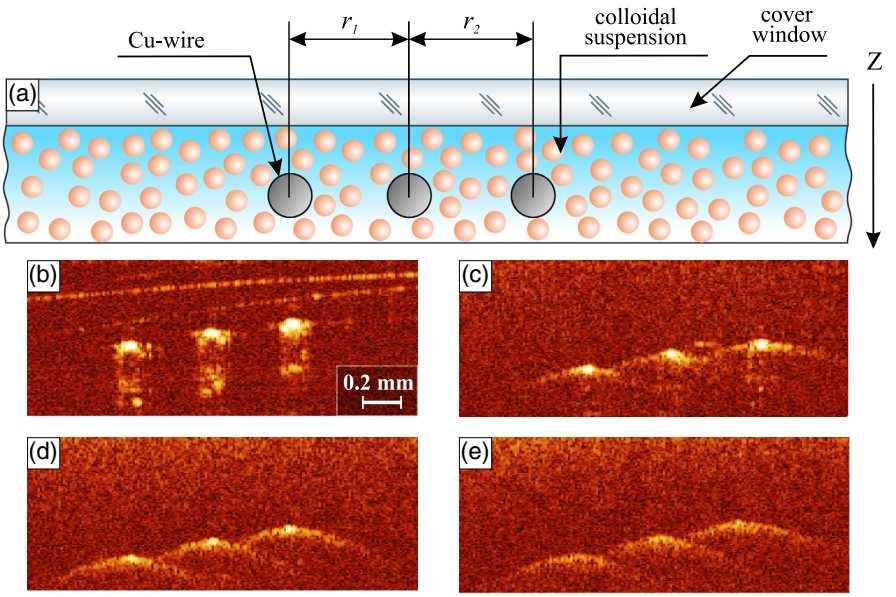

Fig. 1 (a) OCT imaging of the test-object: a scheme of the test-object; (b)–(e) OCT images of the test-object for different concentrations of colloidal suspension of monodisperse nanoparticles $C_0/16$, $C_0/4$, $C_0/2$, and C_0, respectively.

resolution of the OCT system is 50 μm in lateral (A-scan) and 30 μm (B-scan) in depth directions (in the air).

For the experimental training, we prepared four different concentrations of the colloidal suspension: $C = C_0/16$, $C_0/4$, $C_0/2$, and C_0, where $C_0 \simeq 1\%$ is the maximal suspension concentration. Such values were used to demonstrate applicability of the proposed denoising approach in a wide range of scattering parameters, while for the particular object of interest, the scattering parameters should be adjusted precisely as close to the object as possible. OCT imaging of the test-object with these properties yields the results demonstrated in Fig. 1, i.e., the distortions of the OCT images are quite obvious. In particular, strong light scattering in highly concentrated suspension is the reason for distortions and increased background intensity in the image from Fig. 1(e). Moreover, the "wakes," appearing around the metal inclusions in images from Figs. 1(d) and 1(e), can strongly impact the accuracy of estimating the object geometry. At the same time, for the smallest suspension concentration [Fig. 1(b)], the metal inclusions are represented with the sharp intensity peaks. Such distortion of the OCT images complicates analysis and processing of the OCT-imaging data and justifies the importance of introduction of an efficient denoising procedure. These "wakes" might appear as a result of combination of light reflection from metal objects and multiple scattering in the surrounding colloidal suspension. In the case of biological tissues, such artifacts are not expected, and other factors will distort the signal like absorption, surface roughness, or bulk scattering. In general, an effective denoising procedure should suppress these factors and retain information about the object, i.e., interface position, scattering coefficient profile, or position and sizes of the inclusions. For demonstration, we used symmetrical metal objects, assuming that filtration should retain or reconstruct their initial symmetry and thus, the position of center of mass. Depending on the main extracted key features, we could select different criteria and test samples, including ones, accounting for the asymmetric geometry of the sample. For instance, one could use transparent inclusions of spherical or plane form made of glass or plastic.

3 Principle of the Wavelet-Domain Denoising

After registration of OCT images of the test-object, the wavelet filtration of the experimental data is performed. At this stage, various combinations of the wavelet bases and the wavelet-domain filtration procedures are examined in order to select the optimal one.

OCT signal has a form of a spatial distribution of the scattered light intensity $I(x,z)$, where z is a sample depth and x is a lateral coordinate. Wavelet-domain denoising could be separately applied to different cross-sections $x = x'$ of this two-dimensional field, namely, to $I_x(z) = I(x = x', z)$. This procedure includes three main steps.

- Step 1. Direct wavelet transformation:

$$C(a,b) = \mathcal{W}[I(z)] = \int_{-\infty}^{+\infty} I_x(z)\psi(a,b,z)\mathrm{d}z, \tag{1}$$

  where $\psi(z)$ is the mother wavelet and $\psi(a,b,z)$ are the wavelet-decomposition kernels:

$$\psi(a,b,z) = |a|^{-1/2}\psi\left(\frac{z-b}{a}\right), \tag{2}$$

  for which a and b define the scale and the translation, respectively.

- Step 2. Wavelet-domain thresholding:

$$C_T(a,b) = \begin{cases} C(a,b), & \text{if } C(a,b) \geq T, \\ 0, & \text{if } C(a,b) < T, \end{cases} \tag{3}$$

  where T is the threshold value.

- Step 3. Inverse wavelet transformation:

$$I'_x(z) = \mathcal{W}^{-1}[C_T(a,b)] = C_\psi^{-1}\iint_{-\infty}^{+\infty}\frac{C_\mathrm{T}(a,b)}{a^2}\tilde{\psi}(a,b,z)\mathrm{d}a\,\mathrm{d}b, \tag{4}$$

  where $\tilde{\psi}(a,b,z)$ is the dual function of $\psi(a,b,z)$, and

$$C_\psi = \int_{-\infty}^{+\infty}\frac{\Psi(\omega)\tilde{\Psi}(\omega)}{|\omega|}\mathrm{d}\omega < \infty \tag{5}$$

  is the admissible constant restricting the diversity of functions suitable for the definition of the mother wavelet $\psi(z)$. Functions $\Psi(\omega)$ and $\tilde{\Psi}(\omega)$ in Eq. (5) correspond to the Fourier spectra of $\psi(z)$ and $\tilde{\psi}(z)$, respectively.

We implement methods of the fast direct and inverse wavelet transformations (FDWT and FIWT)[58] to force the computations of Eqs. (1) and (4). We consider various wavelet bases from the ones used in FDWT and FIWT algorithms, both "soft" and "hard" thresholding modalities,[59,60] and different number of the decomposition levels L. Each configuration of the wavelet-domain filter is applied to the initial images [see Figs. 1(b)–1(e)], then, using the image thresholding procedure, we determine three image segments with high pixel intensity and find their centroids[61] (i.e., centers of mass). Finally, we estimate the corresponding relative distance for the filtered image $(r_1/r_2)_\mathrm{F}$. This value is compared with the reference one $(r_1/r_2)_0$:

$$d_\mathrm{i} = |(r_1/r_2)_\mathrm{F} - (r_1/r_2)_0|, \qquad i = 1\ldots N, \tag{6}$$

for every i'th of N experiment iterations with the similar object configuration, each of which is characterized by various realization of equal-magnitude noise. The standard deviation (STD) of this estimation is then determined:

$$\sigma_\mathrm{STD} = \left(\frac{1}{N}\sum_{i=1}^{N} d_\mathrm{i}^2\right)^{1/2}. \tag{7}$$

By comparing the σ_STD values based on $N = 5$ measurements, we find the minimal one and the related appropriate wavelet-domain filter configuration. The described experimentally trained wavelet-domain denoising algorithm is summarized in Fig. 2.

4 Choosing the Wavelet-Domain Filter and Application for OCT Imaging

For the described test-object and the corresponding OCT images (Fig. 1), we apply the proposed algorithm. Our database includes 52 mother wavelets of five wavelet families widely applied in FDWT and FIWT algorithms, i.e., daubechies (db),

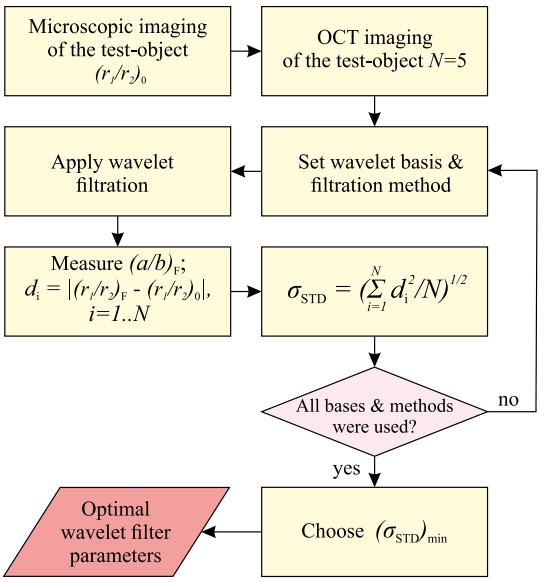

Fig. 2 A scheme of the nanoparticle-enabled experimentally trained wavelet-domain denoising technique, which uses the accuracy of estimating the relative distance between the microscale inclusions r_1/r_2 as a criterion of the noise suppression efficiency.

coiflets (coif), symlets (sym), biorthogonal (bior), and reverse biorthogonal (rbio). We use soft (s) and hard (h) thresholding procedures and four values of L.

Figure 3 shows an error map presented in logarithmic scale $\log(1+\sigma_{STD})$ for different suspension concentrations C. The colormap in this figure is changed from red to dark blue with an increase of the error. By analyzing all values, we selected seven cases, which are marked with blue ovals and correspond to the minimal error below 0.01 from the observed ones. As it is clear from Fig. 3, there is no unique filter configuration with the equally good results for all of the sample concentrations. We could notice that the measurement errors do not depend monotonically on scatterer concentration, which could be due to nonmonotonical changes of the scattering coefficient of turbid media with increased volume fraction of colloidal particles,[62,63] as well as due to complex dependence of the Mie scattering cross-section of microinclusions on the effective refractive index of colloidal suspension.[31] Moreover, when small concentrations of nanoparticles produce weak noise, σ_{STD} has insignificant variations and all considered filter realizations have the similar effect, in contrast to the high concentration with large σ_{STD} variations.

Figure 4 compares seven selected cases of the wavelet-domain filtration. It highlights the concentration influence. When all cases of the sample condition have to be considered, the averaging can help find the appropriate filter parameters. The inset in Fig. 4 demonstrates the mean value $\langle[\log(1+\sigma_{STD})]\rangle_C$. Among these results, we can find that the sixth case bior3.5(4) has better performance for our OCT system and sample. Depending on the goal of OCT imaging, one could increase the number of noise conditions and change the scattering medium.

In order to prove our results, we compare the filtered images for the optimal wavelet filter configuration bior3.5(4) with non-optimal ones (Fig. 5). Configuration sym8(8) corresponds to the highest error among the seven selected cases (Fig. 4); this filter [Figs. 5(i)–5(l)] demonstrates satisfactory speckle reduction but adds dark artifacts and allocates particles' centers at high concentrations less distinctly [Figs. 5(k) and 5(l)] than configuration bior3.5(4). Configuration bior3.3(5) corresponds to the highest error value among all results from our database. Its application [Figs. 5(m)–5(p)] distorts the initial image, adds dark regions

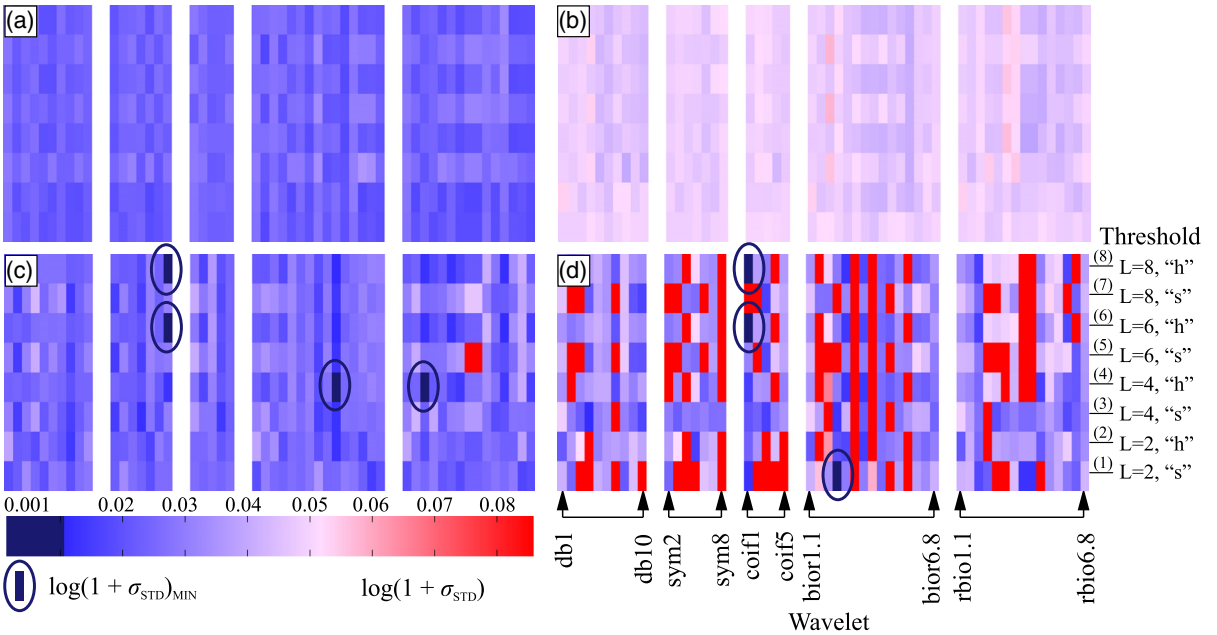

Fig. 3 Wavelet-domain filter selection: (a)–(d) colored diagrams represent errors of $(r_1/r_2)_f$ estimation produced by denoising procedure for the colloidal suspension concentration of $C_0/16$, $C_0/4$, $C_0/2$, and C_0, respectively. Horizontal lines in each panel correspond to eight (1) to (8) different thresholding methods, i.e., soft (s) and hard (h) thresholding procedures and decomposition level L. Vertical lines correspond to 52 mother wavelets of five wavelet families. Seven combinations of filter parameters with lowest errors are marked with dark blue ovals.

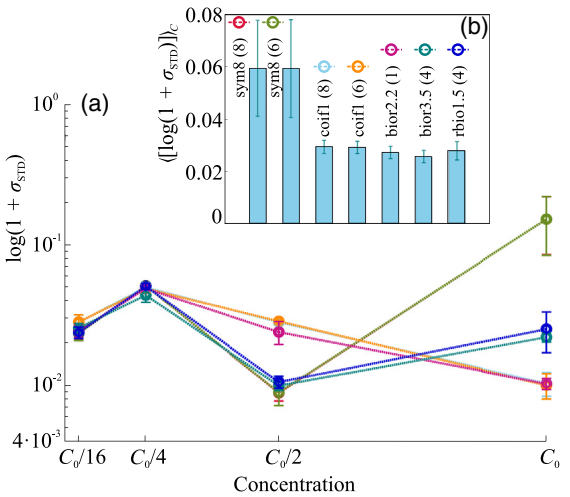

Fig. 4 Analysis of the wavelet-domain denoising performance: (a) a comparison of errors, produced by the seven selected filter parameters and (b) a mean value of error for different suspension concentrations *C*.

and deformations of the sample internal structure. Therefore, bior3.5(4) operates well for both low and high concentrations and confirms the obtained results.

5 Applications of the Denoising Procedure for OCT-Imaging of Meningioma

The latest research demonstrates that OCT could become an effective intraoperative imaging technique for neurosurgery, where fast and accurate detection of tumor margins is of high importance.[14,23,64,65] Recently, numerous modern techniques of tissue imaging are considered to solve this problem: intraoperative magnetic resonance imaging,[66,67] terahertz reflectometry,[68–70] Raman spectroscopy,[71–73] and fluorescence imaging.[74,75] Among them, OCT remains one of the most promising instrument, which yields noninvasive, fast, and label-free 2-D and 3-D visualisation of tissues, providing both lateral and depth information about its structure and scattering properties.

Many biomedical applications of OCT imaging deal with objects featuring finally structured heterogeneous semi-infinite scattering medium with local inclusions possessing high (or low) scattering. Representative examples of this type of objects are tissues of retina,[7] cortex,[12] liver,[24] embryo,[22] and brain.[13] For example, brain meningiomas are characterized by a nonhomogeneous internal structure owing to the presence of cell clusters (whorls) and collagen balls.[13] For the listed tissues, the proposed denoising technique would yield improvement of the OCT image quality, i.e., suppressing the noises and the scattering background, while sustaining and even emphasizing the inclusions, which could serve as specific features of tumorous tissues. Therefore, in order to highlight the potential of the proposed denoising technique for OCT imaging of tissues, we apply the selected wavelet-filter bior3.5(4) for processing the OCT image of the *in vitro* human brain meningioma (Fig. 6).

The sample of brain meningioma tissue [Fig. 6(c)] is explored no later than 4 h after its resection, performed in Burdenko Neurosurgery Institute. To fix the tissue, prevent its hydration/dehydration, and sustain its structure and composition during both transportation and OCT imaging, we place the sample on a reference optically transparent substrate and cover it with gelatin films.[76] The examined tissue sample is excised according to the initial medical diagnosis. After the OCT imaging, it is fixed in formalin and sent to the histological examination, which is aimed to confirm the result of preoperative diagnosis.

The initial OCT image and the denoising data are demonstrated in Figs. 6(a) and 6(b). This example of brain tumorous tissue contains several inclusions of different scale. The large-scale inhomogeneities are quite visible from the initial OCT scan, while scattering noise prevents observation of the small-

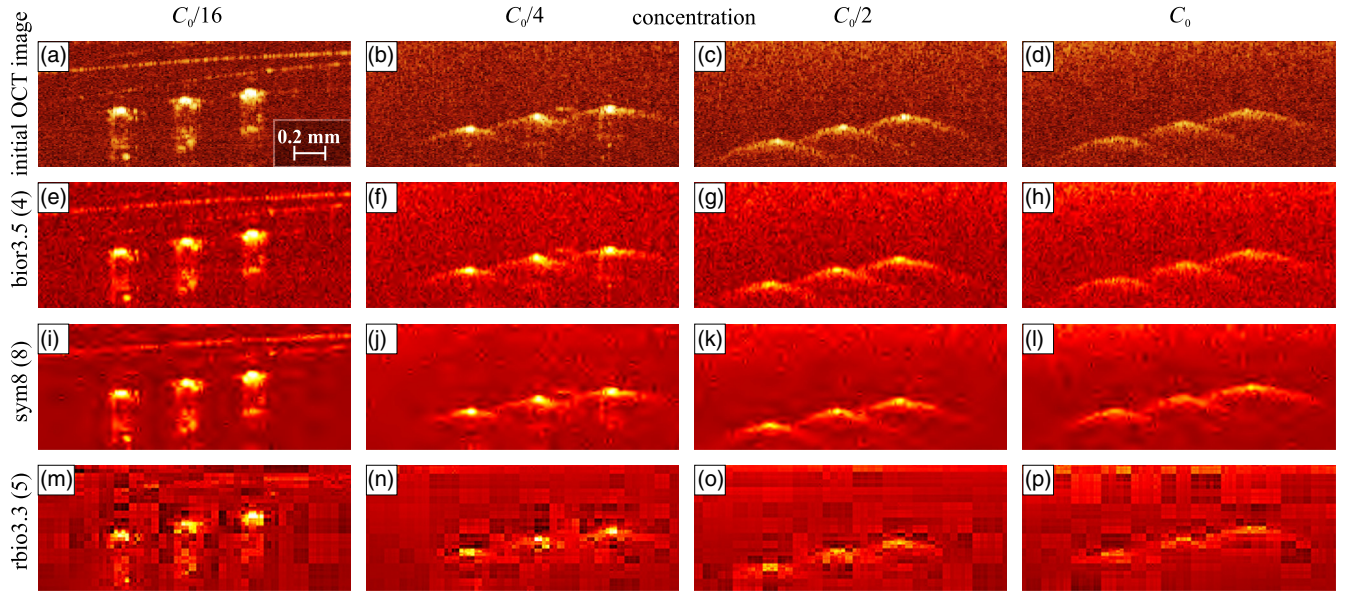

Fig. 5 (a)–(d) Results of wavelet filtration of the initial images (e)–(h) applying the optimal filter parameters, (i)–(l) filtration with one of the seven selected filters with high error, and (m)–(p) the non-optimal filtration with the highest error.

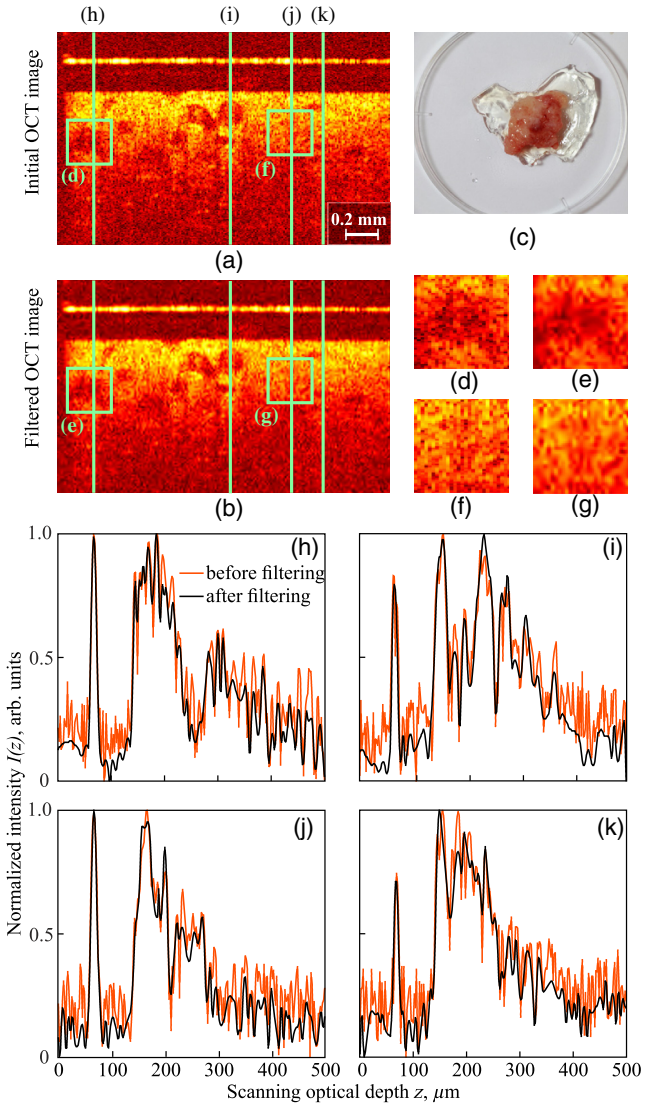

Fig. 6 Application of the wavelet denoising procedure with bior3.5 (4) filter for OCT image of human brain tumor (meningioma): (a) initial and (b) filtered B-scan of the (c) brain meningioma tissue sample; (d) and (f) magnified regions of the B-scan before and (e) and (g) after filtration, respectively; (h)–(k) A-scans before (orange lines) and after (black lines) filtration.

scale ones. Two regions in green rectangles shown on panels [Figs. 6(d)–6(g)] demonstrate an effective denoising inside small circle-like inclusions. This makes the OCT image more sufficient for further segmentation and processing. Moreover, we analyze four vertical cross-sections of the OCT image, marked on both the initial and filtered images. These results are demonstrated in Figs. 6(h)–6(k). Initial intensity of OCT A-scans is shown in red color, and filtered ones are shown in black. It is visible from these panels that the application of the selected wavelet filter leads to noise suppression, while the position and form of all inhomogeneities of tissue are sustained.

6 Discussions

The proposed denoising method could be useful for various OCT applications in biology, medicine, and material science. Despite that we have considered only a representative example of the wavelet-domain denoising, the applied type of nanoparticle test-object can be changed for enabling a better solution for other special denoising problems. The proposed criterion could be effective for training the wavelet-domain filter in such a common case, when we need better detection of microscale inclusions and their relative positions. If other type of data needs to be analyzed from the OCT image, the criterion can be modified according to this purpose. Accordingly, different wavelet filters can become optimal for the same OCT image depending on the extracted information from the object. For example, the experimentally trained wavelet-domain denoising approach could be applied to study the multilayered systems or to measure the scattering parameters of media by solving the OCT inverse scattering problems. However, an appropriate wavelet filter should be constructed to accommodate the needs of the particular OCT application. In further studies, this method would be used for *in vivo* measurements of living tissues, and the test-sample parameters would be corrected significantly.

Furthermore, this method could be generalized for various applications of signal processing, assuming not only the OCT data but also other types of optical and even acoustic signals. Further implementations of the experimentally trained wavelet denoising technique can appear for terahertz pulsed spectroscopy[53,77,78] and time-of-flight tomography,[79] and frequency-resolved optical gating.[80] Moreover, the proposed approach has significant potential for autocorrelation methods[81] applied to measure the ultra-short optical pulses, ultrasonic measurements in biology, medicine, nondesctructive testing,[82,83] magnetic resonance microscopy,[84] etc.

The described method relies on the wavelet analysis, but, in general case, techniques such as fractional Fourier transform and chirplet analysis can be used for optimizing the image decomposition onto a basis of kernels local in both time/space domain and frequency domain. This improvement will lead to accounting for other specific properties of analyzed data, for example, complex internal structure or spectral properties.

The proposed approach of manufacturing the test-object based on colloidal suspension of nanoparticles seems to be useful for solution of the inverse scattering problems in optics, where various methods can be experimentally trained using the prepared test-objects. For example, colloid suspensions of various nanoparticles (amorphous silica, polymers), their mixtures, magnetic materials, and even photonic crystals and amorphous media based on self-assembling from colloid suspension[85] could be applied to simulate, in a simple manner, the media with spatially inhomogeneous scattering properties.

7 Conclusions

In this work, we proposed the nanoparticle-enabled experimentally trained wavelet-domain denoising technique for OCT. The used test-object was manufactured from the aqueous suspension of the colloidal monodisperse nanoparticles and contained the microscale inclusions made of Cu wires. The geometrical and scattering properties of the test-object were determined *a priori* and were used for setting the criteria and adjusting conditions of the training algorithm. The proposed test-object and criterion can be changed according to the stated denoising problem. We used a wide database of wavelet filter parameters for training and determined the most satisfactory filter configuration for the particular OCT measurement conditions. In order to highlight the prospectives of the proposed denoising approach in biology

and medicine, we applied it for the *in vitro* imaging of the heterogeneous tissues—human brain meningiomas. The observed results demonstrated high efficiency of the proposed denoising technique. This general approach could be used for a wide range of applications of biomedical optics and biophotonics.

Disclosures

The authors have no relevant financial interests in this article and no potential conflicts of interest to disclose.

Acknowledgments

Data processing (I.N.D. and N.V.C.) was supported by the Russian Science Foundation (RSF), Project # 14-19-01083. Gelatin embedding of biotissues (S.T.B. and K.I.Z.) was supported by the Russian Science Foundation (RSF), Project # 17-79-20346. Experimental studies (V.V.T.) were supported by the RFBR [17-00-00275 (17-00-00272)] and Government of Russian Federation (074-U01, project 5-100).

References

1. D. Huang et al., "Optical coherence tomography," *Science* **254**(5035), 1178–1181 (1991).
2. V. V. Tuchin, "Tissue optics and photonics: biological tissue structures [review]," *J. Biomed. Photonics Eng.* **1**(1), 3–21 (2015).
3. V. V. Tuchin, "Polarized light interaction with tissues," *J. Biomed. Opt.* **21**(7), 071114 (2016).
4. C. A. Puliafito et al., "Imaging of macular diseases with optical coherence tomography," *Ophthalmology* **102**(2), 217–229 (1995).
5. J. G. Fujimoto, "Optical coherence tomography for ultrahigh resolution in vivo imaging," *Nat. Biotechnol.* **21**(11), 1361–1367 (2003).
6. S. N. Bagayev et al., "Optical coherence tomography for in situ monitoring of laser corneal ablation," *J. Biomed. Opt.* **7**(4), 633–642 (2002).
7. M. Sonka and M. D. Abràmoff, "Quantitative analysis of retinal OCT," *Med. Image Anal.* **33**, 165–169 (2016).
8. M. Cua et al., "Retinal optical coherence tomography at 1 μm with dynamic focus control and axial motion tracking," *J. Biomed. Opt.* **21**(2), 026007 (2016).
9. T. M. Jørgensen et al., "Enhancing the signal-to-noise ratio in ophthalmic optical coherence tomography by image registration– method and clinical examples," *J. Biomed. Opt.* **12**(4), 041208 (2007).
10. J. Aum, J. H. Kim, and J. Jeong, "Effective speckle noise suppression in optical coherence tomography images using nonlocal means denoising filter with double Gaussian anisotropic kernels," *Appl. Opt.* **54**, D43–D50 (2015).
11. A. Lichtenegger et al., "Spectroscopic imaging with spectral domain visible light optical coherence microscopy in Alzheimer's disease brain samples," *Biomed. Opt. Express* **8**(9), 4007–4025 (2017).
12. U. Baran and R. K. Wang, "Review of optical coherence tomography based angiography in neuroscience," *Neurophotonics* **3**(1), 010902 (2016).
13. O. Assayag et al., "Imaging of non-tumorous and tumorous human brain tissues with full-field optical coherence tomography," *Neuroimage* **2**(Suppl. C), 549–557 (2013).
14. K. S. Yashin et al., "Multimodal optical coherence tomography for in vivo imaging of brain tissue structure and microvascular network at glioblastoma," *Proc. SPIE* **10050**, 100500Z (2017).
15. K. S. Yashin et al., "Multimodal optical coherence tomography in visualization of brain tissue structure at glioblastoma (experimental study)," *Sovrem. Technol. Med.* **8**(1), 73–81 (2016).
16. H. Yabushita et al., "Characterization of human atherosclerosis by optical coherence tomography," *Circulation* **106**(13), 1640–1645 (2002).
17. Y. Winetraub et al., "Quantitative contrast-enhanced optical coherence tomography," *Appl. Phys. Lett.* **108**(2), 023702 (2016).
18. J. Welzel, "Optical coherence tomography in dermatology: a review," *Skin Res. Technol.* **7**(1), 1–9 (2001).
19. S. A. Hojjatoleslami, M. R. N. Avanaki, and A. G. Podoleanu, "Image quality improvement in optical coherence tomography using Lucy-Richardson deconvolution algorithm," *Appl. Opt.* **52**, 5663–5670 (2013).
20. I. L. Shlivko et al., "Identification of layers in optical coherence tomography of skin: comparative analysis of experimental and Monte Carlo simulated images," *Skin Res. Technol.* **21**(4), 419–425 (2015).
21. B. G. Muller et al., "Prostate cancer diagnosis: the feasibility of needle-based optical coherence tomography," *J. Med. Imaging* **2**(3), 037501 (2015).
22. L. Zarnescu et al., "Label-free characterization of vitrification-induced morphology changes in single-cell embryos with full-field optical coherence tomography," *J. Biomed. Opt.* **20**(9), 096004 (2015).
23. C. Kut et al., "Detection of human brain cancer infiltration ex vivo and in vivo using quantitative optical coherence tomography," *Sci. Transl. Med.* **7**(292), 292ra100 (2015).
24. Y. Zhu et al., "Rapid and high-resolution imaging of human liver specimens by full-field optical coherence tomography," *J. Biomed. Opt.* **20**(11), 116010 (2015).
25. M. T. Tsai et al., "Differentiation of oral precancerous stages with optical coherence tomography based on the evaluation of optical scattering properties of oral mucosae," *Laser Phys.* **23**(4), 045602 (2013).
26. M. R. N. Avanaki et al., "Investigation of basal cell carcinoma using dynamic focus optical coherence tomography," *Appl. Opt.* **52**, 2116–2124 (2013).
27. V. V. Tuchin, *Handbook of Coherent-Domain Optical Methods*, Springer, New York (2013).
28. M. Wojtkowski, "High-speed optical coherence tomography: basics and applications," *Appl. Opt.* **49**(16), D30–D61 (2010).
29. G. J. Tearney et al., "In vivo endoscopic optical biopsy with optical coherence tomography," *Science* **276**(5321), 2037–2039 (1997).
30. W. Drexler et al., "In vivo ultrahigh-resolution optical coherence tomography," *Opt. Lett.* **24**(17), 1221–1223 (1999).
31. V. V. Tuchin, *Tissue Optics: Light Scattering Methods and Instruments for Medical Diagnostics*, 3rd ed., Vol. **PM 254**, SPIE Press, Bellingham, Washington (2015).
32. N. G. Khlebtsov et al., *Handbook of Optical Biomedical Diagnostics*, Light-Tissue Interaction, 2nd ed., Vol. **PM 262**, SPIE Press, Bellingham, Washington (2016).
33. A. F. Fercher et al., "Optical coherence tomography—principles and applications," *Rep. Prog. Phys.* **66**(2), 239–303 (2003).
34. C. Kasseck et al., "Substance identification by depth resolved spectroscopic pattern reconstruction in frequency domain optical coherence tomography," *Opt. Commun.* **283**(23), 4816–4822 (2010).
35. I. V. Turchin et al., "Novel algorithm of processing optical coherence tomography images for differentiation of biological tissue pathologies," *J. Biomed. Opt.* **10**(6), 064024 (2005).
36. I. I. Fiks et al., "Reconstruction of object location for diffuse fluorescence tomography on the basis of hybrid models of light scattering in biotissues," *Radiophys. Quantum Electron.* **54**(3), 197–209 (2011).
37. J. M. Schmitt, S. H. Xiang, and K. M. Yung, "Speckle in optical coherence tomography," *J. Biomed. Opt.* **4**(1), 95–105 (1999).
38. O. Semyachkina-Glushkovskaya et al., "Laser speckle imaging and wavelet analysis of cerebral blood flow associated with the opening of the blood-brain barrier by sound," *Chin. Opt. Lett.* **15**(9), 090002 (2017).
39. M. Almasian, T. G. van Leeuwen, and D. J. Faber, "OCT amplitude and speckle statistics of discrete random media," *Sci. Rep.* **7**, 14873 (2017).
40. X. Wen et al., "Enhanced optical clearing of skin in vivo and optical coherence tomography in-depth imaging," *J. Biomed. Opt.* **17**(6), 066022 (2012).
41. V. A. Matkivsky et al., "Medium chromatic dispersion calculation and correction in spectral-domain optical coherence tomography," *Front. Optoelectron.* **10**, 323–328 (2017).
42. A. Baghaie, R. M. D'Souza, and Z. Yu, "Application of independent component analysis techniques in speckle noise reduction of retinal OCT images," *Optik* **127**(15), 5783–5791 (2016).
43. F. Luan and Y. Wu, "Application of RPCA in optical coherence tomography for speckle noise reduction," *Laser Phys. Lett.* **10**(3), 035603 (2013).
44. P. Steiner et al., "Automatic estimation of noise parameters in Fourier-domain optical coherence tomography cross sectional images using statistical information," *Appl. Opt.* **54**, 3650–3657 (2015).

45. A. Ozcan et al., "Speckle reduction in optical coherence tomography images using digital filtering," *J. Opt. Soc. Am. A* **24**, 1901–1910 (2007).
46. K.-S. Kim, H.-J. Park, and H. S. Kang, "Enhanced optical coherence tomography imaging using a histogram-based denoising algorithm," *Opt. Eng.* **54**(11), 113110 (2015).
47. D. Alonso-Caneiro, S. A. Read, and M. J. Collins, "Speckle reduction in optical coherence tomography imaging by affine-motion image registration," *J. Biomed. Opt.* **16**(11), 116027 (2011).
48. J. Rogowska and M. E. Brezinski, "Image processing techniques for noise removal, enhancement and segmentation of cartilage OCT images," *Phys. Med. Biol.* **47**(4), 641–655 (2002).
49. D. C. Adler, T. H. Ko, and J. G. Fujimoto, "Speckle reduction in optical coherence tomography images by use of a spatially adaptive wavelet filter," *Opt. Lett.* **29**, 2878–2880 (2004).
50. C. Buranachai et al., "Application of wavelet analysis in optical coherence tomography for obscured pattern recognition," *Laser Phys. Lett.* **6**(12), 892–895 (2009).
51. M. A. Mayer et al., "Wavelet denoising of multiframe optical coherence tomography data," *Biomed. Opt. Express* **3**, 572–589 (2012).
52. A. N. Pavlov et al., "Wavelet-based analysis of cerebrovascular dynamics in newborn rats with intracranial hemorrhages," *J. Innovative Opt. Health Sci.* **7**(1), 1350055 (2014).
53. N. V. Chernomyrdin et al., "Wavelet-domain de-noising technique for THz pulsed spectroscopy," *Proc. SPIE* **9216**, 921611 (2014).
54. W. Stober, A. Fink, and E. Bohn, "Controlled growth of monodisperse silica spheres in the micron size range," *J. Colloid Interface Sci.* **26**(1), 62–69 (1968).
55. A. Zhokhov et al., "Photonic crystal microspheres," *Opt. Mater.* **49**, 208–212 (2015).
56. V. M. Gelikonov et al., "Coherent optical tomography of microscopic inhomogeneities in biological tissues," *JETP Lett.* **61**(2), 158–162 (1995).
57. G. Zuccaro et al., "Optical coherence tomography of the esophagus and proximal stomach in health and disease," *Am. J. Gastroenterol.* **96**(9), 2633–2639 (2001).
58. S. G. Mallat, "A theory for multiresolution signal decomposition: the wavelet representation," *IEEE Trans. Pattern Anal. Mach. Intell.* **11**(7), 674–693 (1989).
59. D. L. Donoho and J. M. Johnstone, "Ideal spatial adaptation by wavelet shrinkage," *Biometrika* **81**(3), 425–455 (1994).
60. D. L. Donoho, "De-noising by soft-thresholding," *IEEE Trans. Inf. Theory* **41**, 613–627 (1995).
61. R. C. Gonzalez and R. E. Woods, *Digital Image Processing*, Prentice-Hall, Inc., New Jersey (2006).
62. J. M. Schmitt and G. Kumar, "Optical scattering properties of soft tissue: a discrete particle model," *Appl. Opt.* **37**, 2788–2797 (1998).
63. E. A. Genina, A. N. Bashkatov, and V. V. Tuchin, "Optical clearing of human dura mater by glucose solutions," *J. Biomed. Photonics Eng.* **3**(1), 010309 (2017).
64. I. N. Dolganova et al., "Wavelet-domain de-noising of OCT images of human brain malignant glioma," *Proc. SPIE* (2018).
65. T. Garzon-Muvdi et al., "Intraoperative imaging techniques for glioma surgery," *Future Oncol.* **13**(19), 1731–1745 (2017).
66. C. Senft et al., "Intraoperative MRI guidance and extent of resection in glioma surgery: a randomised, controlled trial," *Lancet Oncol.* **12**(11), 997–1003 (2011).
67. B. Schatlo et al., "Outcomes after combined use of intraoperative MRI and 5-aminolevulinic acid in high-grade glioma surgery," *Neuro-oncology* **17**(12), 1560–1567 (2015).
68. S. Yamaguchi et al., "Brain tumor imaging of rat fresh tissue using terahertz spectroscopy," *Sci. Rep.* **6**, 30124 (2016).
69. Y. B. Ji et al., "Terahertz reflectometry imaging for low and high grade gliomas," *Sci. Rep.* **6**, 36040 (2016).
70. N. V. Chernomyrdin et al., "In vitro terahertz spectroscopy of gelatin-embedded human brain tumors—a pilot study," *Proc. SPIE* (2018).
71. M. F. Kircher et al., "A brain tumor molecular imaging strategy using a new triple-modality MRI-photoacoustic-Raman nanoparticle," *Nat. Med.* **18**, 829–834 (2012).
72. D. A. Orringer et al., "Rapid intraoperative histology of unprocessed surgical specimens via fibre-laser-based stimulated Raman scattering microscopy," *Nat. Biomed. Eng.* **1**, 0027 (2017).
73. M. Jermyn et al., "Intraoperative brain cancer detection with Raman spectroscopy in humans," *Sci. Transl. Med.* **7**(274), 274ra19 (2015).
74. N. Pustogarov et al., "Hiding in the shadows: CPOX expression and 5-ALA induced fluorescence in human glioma cells," *Mol. Neurobiol.* **54**(7), 5699–5708 (2017).
75. A. A. Potapov et al., "Laser biospectroscopy and 5-ALA fluorescence navigation as a helpful tool in the meningioma resection," *Neurosurg. Rev.* **39**(3), 437–447 (2016).
76. S. Fan et al., "Gelatin embedding: a novel way to preserve biological samples for terahertz imaging and spectroscopy," *Phys. Med. Biol.* **60**(7), 2703–2713 (2015).
77. K. I. Zaytsev et al., "In vivo terahertz spectroscopy of pigmentary skin nevi: pilot study of non-invasive early diagnosis of dysplasia," *Appl. Phys. Lett.* **106**, 053702 (2015).
78. K. I. Zaytsev et al., "Accuracy of sample material parameters reconstruction using terahertz pulsed spectroscopy," *J. Appl. Phys.* **115**(19), 193105 (2014).
79. K. I. Zaytsev et al., "Invariant embedding technique for medium permittivity profile reconstruction using terahertz time-domain spectroscopy," *Opt. Eng.* **52**(6), 068203 (2013).
80. R. Trebino et al., "Measuring ultrashort laser pulses in the time-frequency domain using frequency-resolved optical gating," *Rev. Sci. Instrum.* **68**(9), 3277–3295 (1997).
81. H.-C. Lihn et al., "Measurement of subpicosecond electron pulses," *Phys. Rev. E* **53**, 6413–6418 (1996).
82. F. Foster et al., "Advances in ultrasound biomicroscopy," *Ultrasound Med. Biol.* **26**(1), 1–27 (2000).
83. C. R. Hill, J. C. Bamber, and G. R. ter Haar, *Physical Principles of Medical Ultrasonics*, 2nd ed., John Wiley & Sons Ltd., England (2005).
84. P. Glover and S. P. Mansfield, "Limits to magnetic resonance microscopy," *Rep. Prog. Phys.* **65**(10), 1489–1511 (2002).
85. E. V. Yakovlev et al., "Tunable two-dimensional assembly of colloidal particles in rotating electric fields," *Sci. Rep.* **7**, 13727 (2017).

Irina N. Dolganova received her PhD in engineering sciences. Currently, he is a researcher in the Institute of Solid State Physics of Russian Academy of Sciences, Chernogolovka, Russia (ISSP RAS) and a researcher and an associated professor at Bauman Moscow State Technical University (BMSTU), Moscow, Russia. Her research interests include optics and biophotonics, light scattering, optical coherence tomography, and denoising of optical signals.

Nikita V. Chernomyrdin is currently a researcher at A.M. Prokhorov General Physics Institute of Russian Academy of Sciences, Moscow, Russia (GPI RAS) and a researcher and an assistant professor at BMSTU Moscow, Russia. His research interests include biomedical optics, applications of terahertz technologies for medical diagnosis, and high-resolution terahertz imaging systems.

Polina V. Aleksandrova is currently a student at BMSTU Moscow, Russia. Her research interests include optical coherence tomography, biomedical optics, and OCT denoising methods.

Sheykh-Islyam T. Beshplav is currently a clinical resident of Neurooncology Department at Burdenko Neurosurgery Institute. His research interests include corpus callosum, brain tumors, 5-ALA fluorescence, terahertz biomedicine, and optical coherence tomography.

Alexander A. Potapov is a professor of neurosurgery and a director of Burdenko Neurosurgery Institute, Moscow. His research interests include brain tumors, brain trauma, fluorescence, and spectroscopy.

Igor V. Reshetov is a doctor of medical sciences, a corresponding member of the Russian Academy of Sciences. Currently, he is a professor at I.M. Sechenov First Moscow State Medical University, Moscow, Russia (FMSMU) and a practicing surgeon. His research interests include plastic and reconstructive microsurgery in oncology, head and neck tumors, including technologies for treatment, reconstruction, rehabilitation, and development of novel technologies for medical diagnosis of human body malignancies.

Vladimir N. Kurlov received his Dr. Sci. degree in engineering sciences from the National University of Science and Technology MISIS,

Moscow, Russia, in 2004. He is the head in the Shaped Crystal Growth Laboratory at the Institute of Solid State Physics of Russian Academy of Sciences (ISSP RAS), Chernogolovka, Russia. His research interests include crystallography, bulk and shaped crystal growth technologies, including, sapphire and other oxide crystals, and applications of crystals in optics and biomedical sciences.

Valery V. Tuchin is a professor and head of optics and biophotonics at Saratov State University (National Research University of Russia) and several other universities. His research interests include tissue optics, laser medicine, tissue optical clearing, and nanobiophotonics. He is a fellow of SPIE and OSA. He has been awarded Honored Science Worker of the Russia, Honored Professor of Saratov University, SPIE Educator Award, FiDiPro, Finland, Chime Bell Prize of Hubei Province, China, NanQiang Life Science Series Lectures Award of Xiamen University, China, and the Joseph W. Goodman Book Writing Award (OSA/SPIE).

Kirill I. Zaytsev received his PhD in engineering sciences. Currently, he is a head in the laboratory at A.M. Prokhorov General Physics Institute of Russian Academy of Sciences, Moscow, Russia (GPI RAS) and a researcher and an associated professor at BMSTU Moscow, Russia. His research interests include optics and biophotonics, inverse problems in optics, dielectric spectroscopy, terahertz science and technology, and computational electrodynamics.